Chapter 3
Dynamic Analysis and Design of Turbine

Under the action of the Kuroshio, the turbine anchored by a single cable on the relay platform shall experience complicated reaction to the strong current, among which the displacement of the turbine swift with the current, the deformation of the turbine body due to the forces applied by the current, and the vibration of the turbine due to the dynamic effects in various respects are all important problems to be solved to make a turbine of great power efficiency. On the other hand, the power efficiency of turbine correlates closely with its structure stiffness. To analyze the stiffness of the turbine, one shall investigate the reaction force applied on each component of the turbine, the dynamical effects due to the vortex shedding generated from rotor, the high-frequency force variation due to the turbulence, the impact due to the phase difference between rotors, and the cavitation possibly occurring on the rotor blade so that the design of turbine can be carried out. In this chapter, we employ the computational fluid dynamic to explore the time-dependent dynamic forces applied on the turbine under the action of the Kuroshio, and the results are compared with those obtained by blade element momentum (BEM) theory to confirm the accuracy of the CFD results.

As mentioned in Chap. 2, the reasons to choose GST to deploy in the Kuroshio are that it has a tail-wing stabilizer to autonomously adjust the turbine altitude to face against the current, and it can be anchored on the relay platform with a single cable. Two reversely rotating rotors are installed at the nose of watertight nacelles, which are connected with the main pontoon by several connecting linkages. The front view of the turbine looks like a triangular configuration, as shown in Fig. 3.1. Given the characteristics of the Kuroshio and the power generation requirements in mind, we made some minor changes to the original GST design [1]. For example, the length of the axial ratio for the main pontoon and the two watertight nacelles was changed to 3:1 for elliptical streamlining, the cross section of the connecting linkage with the anchor joint was changed to an aspect ratio of 2:1, a NACA4415 airfoil is chosen to be the blade of the rotors, and so on.

As one can see from Fig. 3.1, we decided to use two three-blade rotors for the turbine because, in general, increasing the number of the blades will end up with a lower rotational speed, but will enlarge the bearing torque and increase the costs of

F. Chen, *The Kuroshio Power Plant*, Lecture Notes in Energy 15,
DOI 10.1007/978-3-319-00822-6_3,

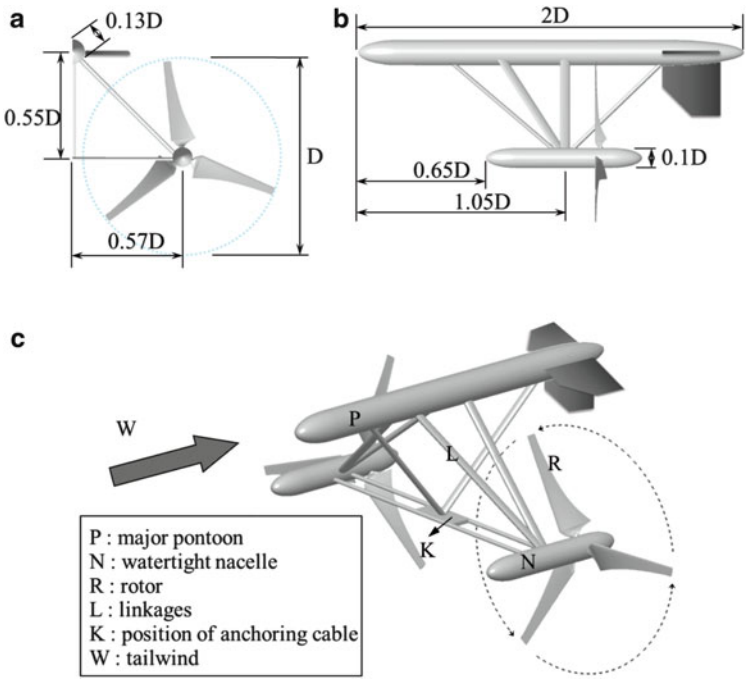

Fig. 3.1 The schematic drawing of the GST (modified after [1]). (**a**) Front view (half-symmetry model). The GST has two sets of three-bladed rotors connected with a pontoon in a *triangular* configuration. (**b**) Side view. A 2*D* length main pontoon and two 1*D* length watertight nacelles are connected by the connecting linkages. Note that D is the diameter of the rotor. (**c**) Perspective view. The main pontoon is at the *top center* of the turbine, the two nacelles are placed on the two sides of the turbine, and the anchoring point is at the *bottom center*. The linkages connect the pontoon and the watertight nacelles. Note that in the computation the tail-wing stabilizer is not taken into account

manufacture and maintenance as well. On the other hand, decreasing the number of the blades increases the rotational speed, resulting in higher noise and vibration. Consequently, as concluded by numerous studies from different perspectives, a three-blade rotor shall reach an optimizing situation of reasonable rotation speed with a higher power output without producing annoying noise or vibration [1, 2].

The optimized design for the blade is to ensure that the torque applied on the blade shall be constant in the radial direction. As a result, the pitch angle, the twist angle, and the chord length of the blade shall vary in the radial direction so that the interaction between the blade and the current can be done under the most efficient angle of attack and a maximum contact area. To meet the requirements above, the airfoil NACA4415 is selected. A special attention is paid to the design for the base of the blade, which locates within $r/R < 0.1$, where r is the distance from the blade to the rotor center and R is the rotational radius. The base serves to hook the blade on the hub of the rotor and is designed to change the shape from the airfoil to a circular cylinder, so that the blade can be strong enough to cope with the largest

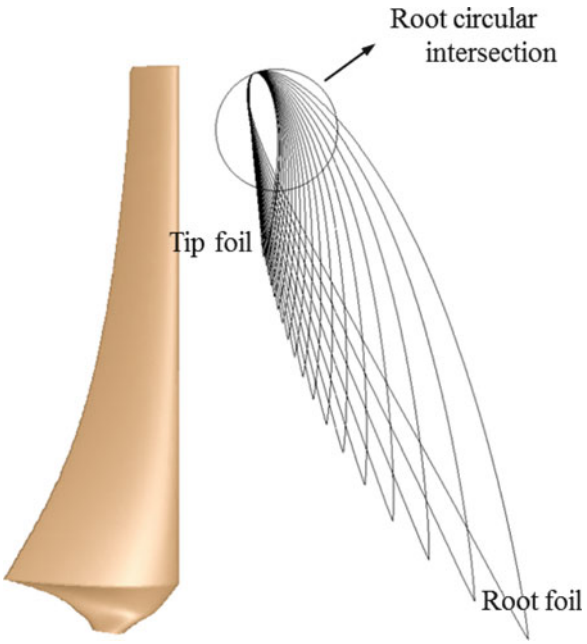

Fig. 3.2 The schematic drawing of the cross section of the blade. Based on the NACA4415 airfoil data, the pitch angle, the twist angle, and the chord length are varied along the radial direction of the blade. The cross section of the blade base is changed from an airfoil at the blade tip to a cylinder at the blade root

torque ever occurring at the turbine. In addition, an optimal tip speed ratio (TSR) with the number of blade, the size, and the cross-sectional shape is also prerequisite for the analysis. We referred to the design of SeaGen of MCT company [2] and determined the following design parameters: A three-blade rotor with blade length of 10 m, a hub of a diameter 2.3 m, and a rated TSR of 5. Consequently, the schematic drawing of the blade shape is shown in Fig. 3.2.

3.1 Physical Models and Numerical Schemes

As shown in Fig. 3.1, the turbine can be divided into the fuselage (including the main pontoon and the watertight nacelles), the connecting linkages, and the rotors. Given the right–left symmetry of the body, the computational effort can be saved significantly by only considering the right half of the turbine in the analysis. Besides, given this symmetry, the tail stabilizer can be excluded from the computation momentarily. We accordingly assume that the turbine shall remain the designed altitude facing against the current without being disturbed by flow turbulence. Finally, the design of the tail-wing stabilizer will be taken into account based on the forces applied on the turbine's components obtained by previous computations.

In present computational work, a computer-aided design (CAD) software is used to build a geometric model of the turbine. We then computed the grid division and demarcation and ended up with a computational grid, which is then used as an input to the CFD code named ANSYS Fluent [3] to discretize the governing equations and boundary conditions. The governing equations are conservation equations of mass and momentum [4, 5]. The Reynolds-averaged Navier–Stokes equations (RANS) are employed to take the turbulent effect into account. As a result, the eddy viscosity is generated in the equation and is simulated by using the so-called $k - \omega$ model [6, 7], where k is the turbulence kinetic energy and ω is the specific dissipation rate.

To discretize the governing equations, we select a second-order upwind difference scheme and employ the slow-converging pressure-based segregated algorithm to reduce the size of memory required for efficient computations. The pressure correction equation is solved by using the semi-implicit method for pressure-linked equations (SIMPLE) proposed by Patankar and Spalding [8]. Transient phenomena are dealt with a sliding mesh (SM) which is based on implicit time discretization to derive unconditional stability for all time steps.

Figure 3.3 shows the final computational grid. The computational domain is enclosed by a half cylinder (symmetrical model) where the diameter of the cylinder is ten times the diameter of the rotor (i.e., $10D$). The gravity center of turbine locates at the center of the computational domain and is at a distance of $5D$ from the left boundary and $12D$ from the right boundary of the computational domain. Consequently, the total number of nodes is about 1.5 million (or 1.5 M). Special attention shall be paid to the grid surrounding the rotor. To simulate the rotation of the rotor, the grid surrounding the rotor is separated with the remaining grid to form a domain of a circular plate; see the yellow grid in Fig. 3.3. The computation moves forwards with a proper speed so that the circular-plate grid will rotate in the same phase with the rotor. Consequently, the nodes inside and outside the circular plate shall coincide with each other at each time step.

Before carrying out the entire analysis, we conducted a grid independency test by considering three different grids, which have, respectively, 1.5 M, 3.3 M, and 7.0 M nodes. Results show that, for the three cases considered, the difference between the results lies within a range from 0.57 % to 5.32 %, implying that a larger number of grid nodes do not mean to get a more accurate result, while the computational effort for 7.0 M case is many folds larger than the 1.5 M case. Accordingly, the grid of 1.5 M nodes will be used for the cases considered in this study.

3.2 Typical Flow Field

In the computation, the incoming flow is assumed to be a laminar flow of a velocity 1.4 m/s. While the flow passes through the turbine, complicated and unstable variations will be generated under the action of the rotor blades. A typical flow

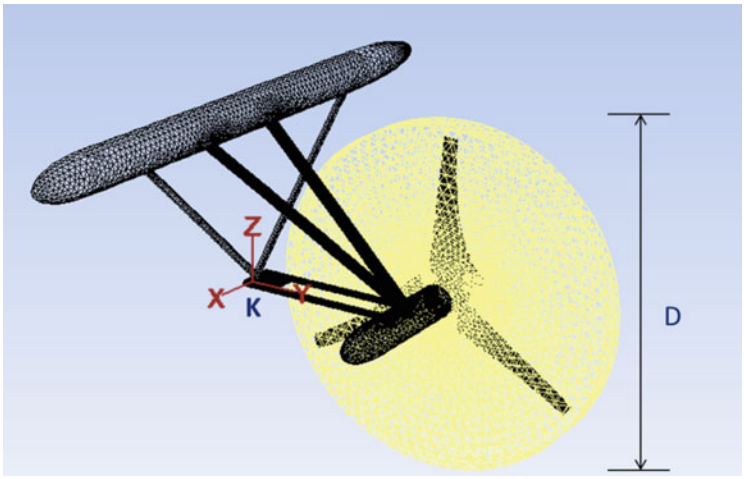

Fig. 3.3 The half-symmetrical computation domain and grid are shown. The total number of the grid nodes is about 1.5 M. A cylindrical offset rotating domain rotates with the three-blade rotor. In the calculation, the half-symmetrical model is employed without considering the tail-wing

for the case of rotor's angular speed being 6 rpm is shown in Fig. 3.4, where the flow animation illustrates the position change of a row of flow particles (white balls) perpendicular to the rotor axis passing through the turbine. As shown in Fig. 3.4a–f, the particles behind the rotor experience a serious lag behind those away from the rotor, implying that the flow momentum behind the rotor is decreased and the wakes are generated behind the rotor. The flow far away from the rotors retains most of the momentum of the inflow, virtually not affected by the rotor. The loss of linear momentum is converted to angular momentum by the rotor to drive the power generator. As a result, a higher loss of momentum in the wake leads to a higher efficiency and better performance of the turbine. As shown in Fig. 3.4, the momentum loss in the wake accounts for a large portion of the total momentum of the incoming flow, implying that the present design of the rotor is of high efficiency and the turbine is of good performance, which will be confirmed by the discussions in the following sections.

According to the conceptual design shown in Chap. 2 (see Fig. 2.1), the Kuroshio power plant is assembled by dozens of turbines arranged in a way of staggered matrix. The space between turbines is determined based on the principle that the adjoining turbines cannot interfere with each other and the wake generated by the turbine at front cannot affect the performance of the turbine at behind [9–14]. As a result, in the direction perpendicular with the flow, the distance between turbines can be arranged to be $2D$–$3D$. In the direction parallel to the flow, the distance between turbines shall be as large as $5D$–$10D$, depending on the flow velocity and the rotor's angular speed [15].

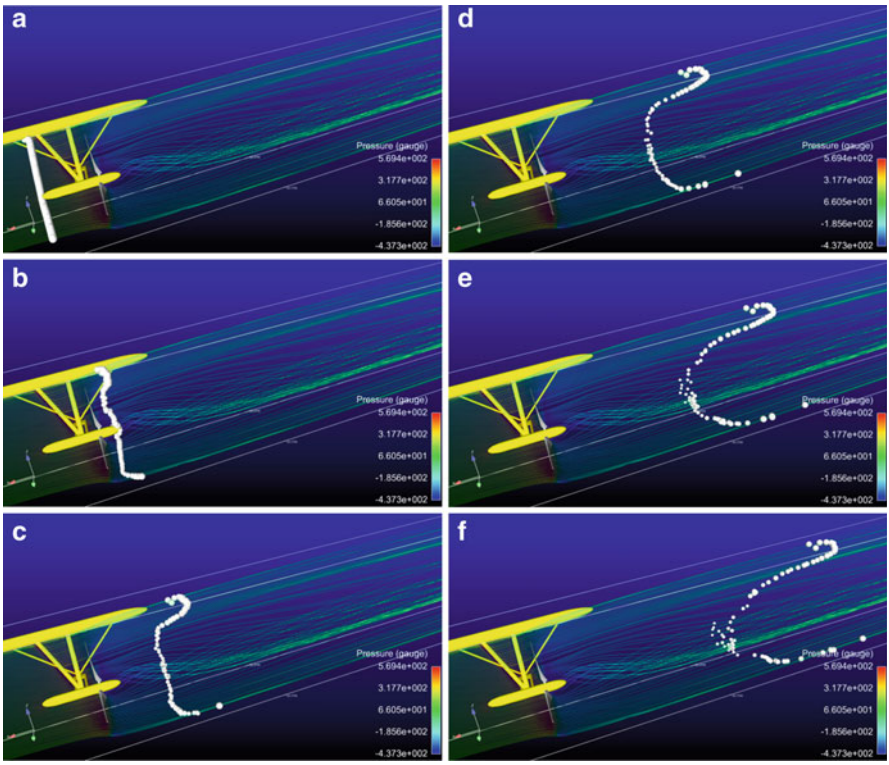

Fig. 3.4 The flow field animation of the current running through the turbine. The row of flow particles (*white balls*) shows (**a**) the flow precedent to the turbine; (**b**) the flow is passing the rotor; (**c–f**) the flow behind the rotor moves much slower than that far away from the rotor

3.3 Reaction Force on the Turbine

After referred to the parameter analyses and results of previous studies [15–19], we consider for the following cases the flow velocity to be 1.4 m/s and the blade rotation speed to be 6 rpm to fit the optimal operating condition of GST. Figure 3.5 shows the reaction forces of the GST in three axial directions, which vary with the phase angle of the blades. As shown in Fig. 3.3, we set the origin of the Cartesian coordinate system at the center of based connection linkage, noted as the anchor point K on which the cable is fixed. The flow moves along the *X*-axis, the *Z*-axis stands for the vertical axis perpendicular with the flow, and the *Y*-axis stands for the horizontal axis perpendicular with the flow. The three curves depicted in Fig. 3.5 show the force changes three times in the *Y*-direction and six times in both the *X*- and *Z*-directions, while all vary periodically with the blade rotation. In the direction of the flow (i.e., the *X*-axis), the force is 365 $\pm$ 10 kN (1 KN means 10**3 Newton), while the respective forces in the *Y*- and *Z*-axes are 5 $\pm$ 3 kN and 7 $\pm$ 2 kN. The force in the *X*-axis is considerably larger than those in the other two

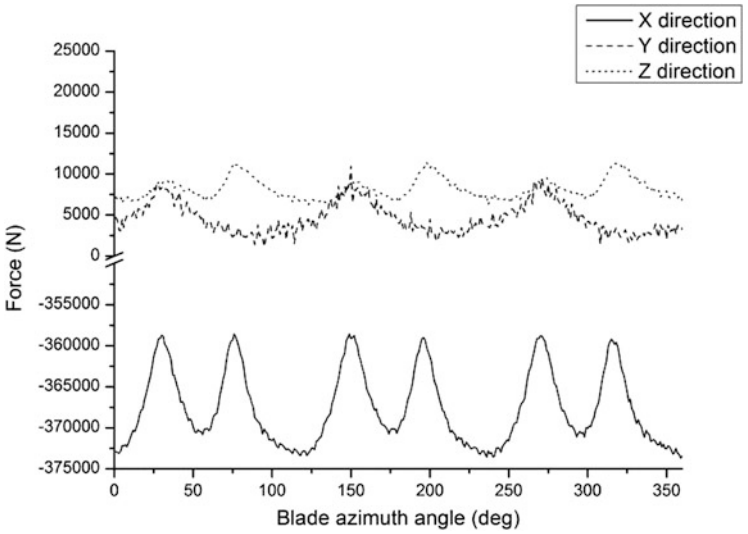

Fig. 3.5 The forces in three axial directions exerted on the single-rotor turbine with different blade azimuthal angles. Force is largest in the *X*-direction (*bottom curve*), about 40–50 times the force in the *Y*- and *Z*-directions (*top two curves*). For the normal twin-rotor turbine, the actual forces shall be twice as large as the ones shown in the figure

axes due to the fact that the blades absorb the vast majority of the flow's kinetic energy, implying that the present GST is a good design of high efficiency. Note please that the present computation is done for a single-rotor turbine due to the symmetric situation considered. As soon as the normal twin-rotor turbine is considered, the forces shown in Fig. 3.3 shall be multiplied by two to account for the overall force exerted on the turbine.

The periodical variation of the force exerted on the turbine is a result from the fact that the forces exerted on the three blades vary periodically with time. As shown in Fig. 3.6, the force exerted on blade 1, for example, exceeds 118 kN when the blade passes through the angle at 150° and then drops to 105 kN twice before the blade returns to 150°. This is because the blade passes consecutively through the wakes generated behind the connecting linkage 3 (and linkage 4) and the base linkage (see Fig. 3.1), resulting in a periodic reduction of power output of turbine which is referred to as the so-called tower shadow effect. Similar results are also found for the other blades. The reduction of the exerted force on each blade due to the tower shadow effect is about 12 % of the force in *X*-direction, which may cause structure damage and power reduction. This, however, cannot be prevented as long as the rotor is set behind the connecting linkages.

The time variations of the force exerted on the other turbine components are plotted in Fig. 3.7. It shows that the maximum forces occur on linkages 1 and 2, and then the forces on linkage 3, the base linkage, linkage 4, and finally the minimum

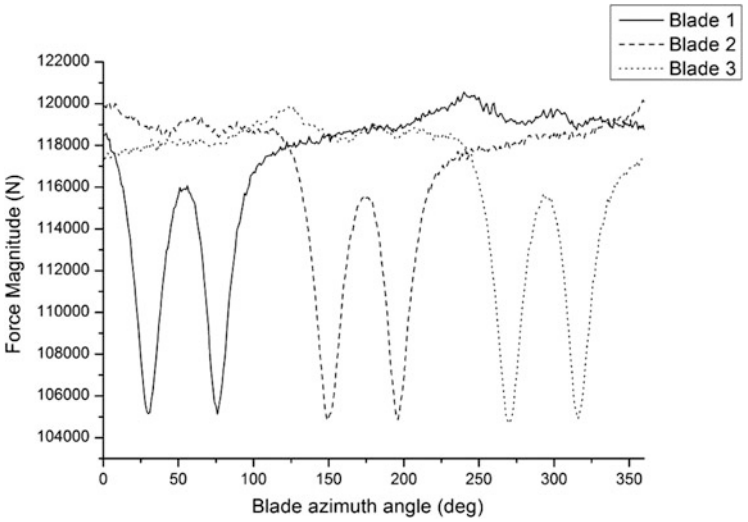

Fig. 3.6 The cyclic variations of the force exerted on each blade. On each blade, the force experiences twice the force reduction because the blade passes through two wakes behind the two linkages

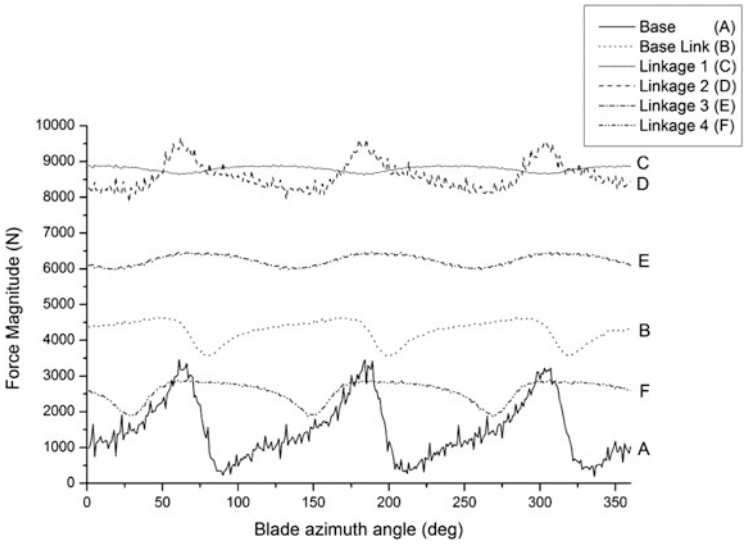

Fig. 3.7 The cyclic variations of the force exerted on each linkage

force occurs on the base. The periodical variation of the force exerted on linkage 2 is apparently due to that it sits within the wake generated by linkage 1. Similar reason can be applied for that the force exerted on linkage 3 is greater than that on linkage 4. That the force exerted on linkages 1 and 2 is greater than that of linkages

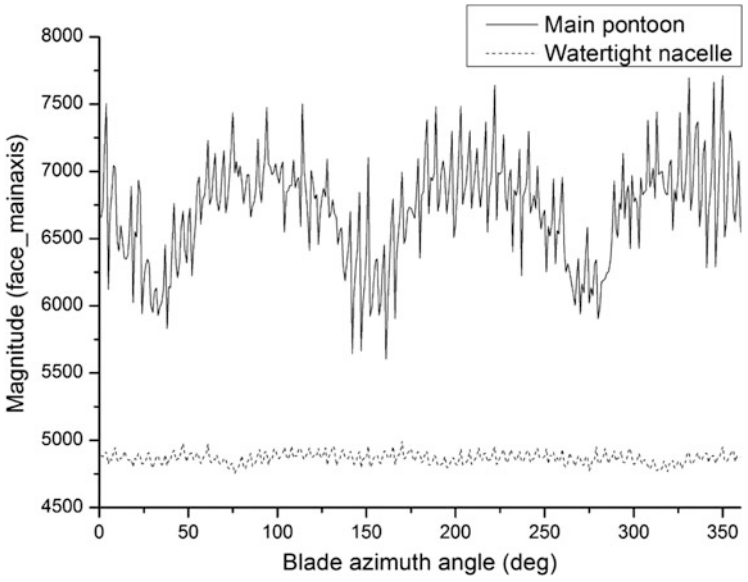

Fig. 3.8 The cyclic variations of the force exerted on the main pontoon and the watertight nacelle

3 and 4 is because the flow velocity is larger when passing through the region between two rotors than when flowing into the rotor regimes. The force exerted on the base point is the smallest because the cross area facing the flow is the smallest, resulting in a smallest resistance force to the flow. Nevertheless, the reaction forces on these linkages are only about 3 % of those on the blades in the *X*-direction, showing that the streamline shape of the cross section of these linkages has successfully reduced the resistance to the flow.

Also shown in Fig. 3.8 are the force variations on the main pontoon and the watertight nacelle. It is seen that the averaged forces on pontoon and nacelle are about 6.7 kN and 4.8 kN, respectively, being about the same magnitude with those on the linkage. Although the size of pontoon or nacelle is much larger than that of linkage, the forces exerted on these components are virtually of the same magnitude, implying that the streamline shape of pontoon and nacelles works successfully to reduce the resistance on the flow. On the other hand, because both the diameter and length of the main pontoon are larger than those of watertight nacelle, a larger reaction force and a greater wake-induced force fluctuation occur on the pontoon. But, after all, this high-frequency force fluctuation of both pontoon and nacelle is negligible comparing with those on the blade.

We categorize the components of the turbine into blade, linkage, and hull and sum up the forces on each of them, and the results are shown in Fig. 3.9. It is seen that in the *X*-direction the force on the blade accounts for more than 93 % of the total force on the turbine. The other parts of turbine, i.e., the five linkages, one pontoon, and two nacelles, are loaded with less than 7 % of the total force. Similar results are found in the other two directions, although the percentage of the total

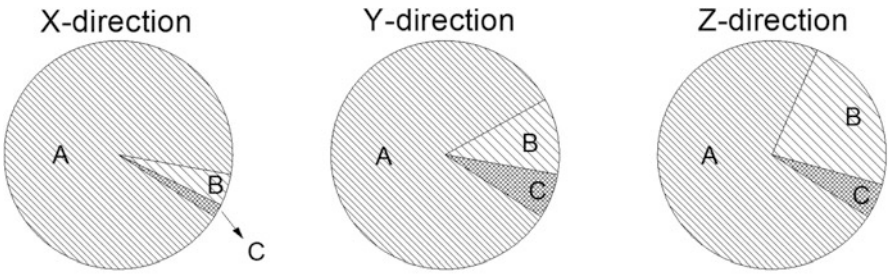

Hydrodynamic force distribution			
	X-direction	**Y-direction**	**Z-direction**
Blade (A)	344135.06 (93.62%)	42615.85 (82.78%)	41937.91 (72.36%)
Linkage (B)	16535.64 (4.5%)	5570.14 (10.82%)	13163.44 (22.71%)
Hull (C)	6910.34 (1.88%)	3295.20 (6.40%)	2858.41 (4.93%)

unit: N

Fig. 3.9 Force exerted on each GST component. The force on blades accounts for a great majority of force exerted on GST in all directions. The proportion of the force on the connecting linkages and fuselage increases slightly in the *Y*- and *Z*-directions

force on the turbine body is larger due to the smaller magnitude of the forces on the blade than that in the *X*-direction. It is also seen that, in all three directions, the forces exerted on linkages and hull are much smaller than those on the blades, showing that the present design of turbine body meets the requirement to reach a high efficiency. On the other hand, the forces on the blades are dominated by that in the *X*-direction, which is about eight times larger than those in the other two directions, also showing how a good design of turbine shall be. The forces on linkages and hull, nevertheless, are of the similar magnitude in all three directions, showing that the present design has no directional preference with respect to the incoming flow.

3.4 Turbine Performance

The performance of turbine is evaluated through three aspects, i.e., the power output, the shaft torque, and the thrust. By and large, the power output directly reflects the amount of kinetic energy captured by the rotor, the shaft torque directly impacts the power output, and the thrust influences the magnitude of shaft torque. Their values are interdependent and vary with the velocity of the incoming flow [20]. In this section, we discuss on the influence of the flow velocity on the turbine performance.

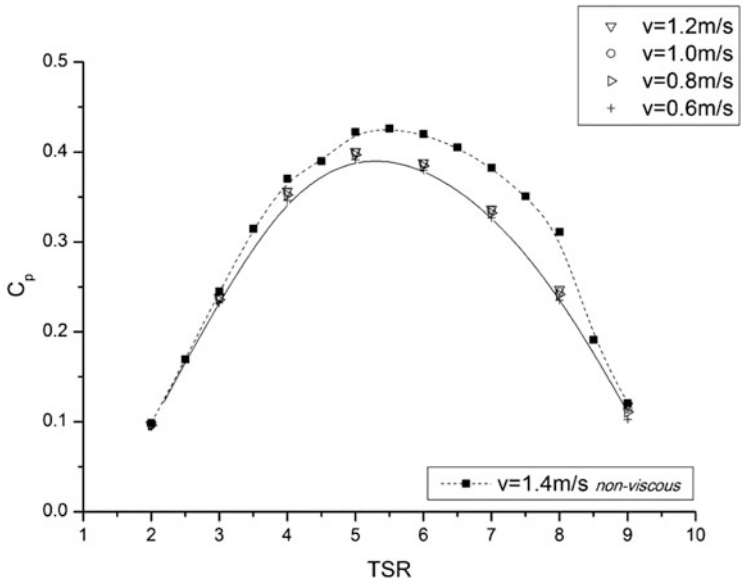

Fig. 3.10 The relation between TSR and C_p for the rotor of GST under four different inflow velocities U and a constant shaft angular velocity Ω

To investigate the dependence of the turbine performance on the flow velocity, the relation between the TSR and the power output coefficient C_p of the rotor shall be illustrated. The TSR is the ratio of the tangential velocity at the blade tip to the inflow velocity, defined as TSR $= \Omega R/U$, where Ω is the shaft angular velocity, $R = D/2$ is the distance between the blade tip and the center of the shaft (or the radius of the rotor), and U is the inflow velocity. If P is the power output, then the power coefficient is defined as $C_p = 2P/\rho U^3 A_{eff}$, where ρ is the seawater density, and A_{eff} is the effective area of the rotor. Accordingly, TSR can represent the variation of C_p in different values of U (or Ω) for a constant Ω (or U).

In Fig. 3.10, we show the TSR–C_p curve for the rotor of GST, in which four different flow velocities, $U = 0.6$, 0.8, 1.0, and 1.2 m/s with a constant shaft angular velocity Ω are considered. Interestingly, all these four curves show that the maximum C_p occurs at TSR $\fallingdotseq 5$, implying that the rotation speed of rotor shall change with inflow velocity to maintain TSR $\fallingdotseq 5$, which is by no means an easy job because, in reality, the velocity of the Kuroshio fluctuates with time. Accordingly, a powerful electronic control unit shall be installed within the generator to control the rotation speed of the rotor to achieve the design value of TSR $\fallingdotseq 5$ under varying inflow velocity.

Figure 3.11 shows the power output of the GST rotor under the conditions $U = 1.4$ m/s, $\Omega = 6$ rpm, and $R = 11.15$ m. Results show the power output varies periodically because of the tower shadow effect explained in Sect. 3.3. The maximum power output can be as high as 245 kW and the minimum is about 225 kW, giving an average value of power output about 235 kW, which is for a single rotor.

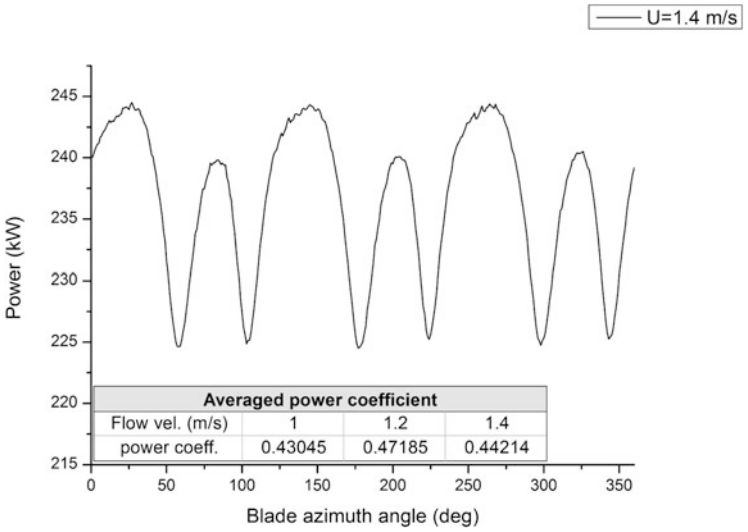

Fig. 3.11 Turbine output power fluctuates with the blade azimuthal angle

For GST a turbine of two rotors, the average power output can be 470 kW, and the maximum power output can be as high as 490 kW.

The results of Fig. 3.10 obtained by CFD can be verified by the cubic relation between the power output and the flow velocity. For TSR $= 5$ with $U = 1$ m/s and $\Omega = 4.28$ rpm, the single rotor average P is about 88.83 kW, which is about 0.38 times that of $U = 1.4$ m/s, fitting well with the theoretical relationship that $P \sim U^3$.

3.5 Dynamic Effects

The design of GST is endowed with several dynamical phenomena which may influence significantly the performance of the turbine. They are, for example, the tower shadow effect due to the wake impinging on the rotor, the turbulence effect due to the flow fluctuation, the dual-rotor effect due to rotors operated in different phase, the cavitation effect due to the exceeding rotor speed, and so on. We shall discuss these effects on the turbine performance in the following.

3.5.1 Tower Shadow Effect

As shown in Figs. 3.5, 3.6, 3.7, and 3.8, the forces exerted on GST components vary periodically with time, resulting in the fluctuation of the power output as shown in Fig. 3.11. As explained in Sect. 3.3, this is clearly a result from that

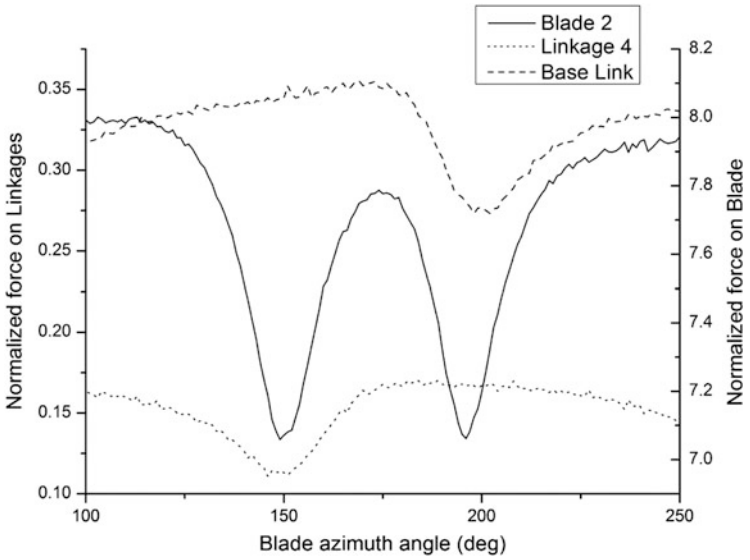

Fig. 3.12 The normalized force exerted on the blade and linkages changes periodically with blade azimuthal angles

the wakes generated by the two sets of connecting linkages impinge on the rotor, commonly known as the tower shadow effect. Figure 3.5 shows that the force in X-direction experiences six undulations of an amplitude about ± 3 % of the total force in one revolution of rotation. The force in Z-direction also experiences six undulations. But the force in Y-direction experiences only three undulations because the wake effects on the two rotors are offset due to the right–left symmetry.

To illustrate the tower shadow effect on GST, the variations of the normalized forces, defined as $C_{Fi} = 2F_i/\rho U^2 A_{\text{effi}}$, exerted on blade 2, linkage 4, and the base linkage are shown in Fig. 3.12, where F_i and A_{effi} are the force and effective area of the turbine component. Results show that the normalized force on base linkage is about twice as large as that on linkage 4, which is because the cross-sectional area of base linkage is larger. The force on linkage 4 experiences a drop at the blade azimuthal angle at 149° when the blade is passing behind the linkage. This is because the impedance on the flow due to the rotor at behind reduces the force exerted on the linkage. Similarly, the force on base linkage experiences a drop at the angle of 196° under the same reason. On the other hand, a combination of above two force-drops leads to that the blade 2 experiences two force-drops at respectively 149° and 196° due to the wakes generated by the base linkage and the linkage 4 [13, 14].

3.5.2 Turbulence Effect

Figure 3.5 shows the turbine is not only subject to the low-frequency force variations due to the tower shadow effect, but also subject to the high-frequency force variation of smaller amplitude caused by the turbulence effect. It is seen that, although the turbulence effect is seen at almost every blade angle, the effect is more obvious when it rotates to the downstream of linkage 4 and base linkage. The variation due to turbulence effect is largest in the Y-direction (about $\pm$1,500 N). In the X-direction, the turbulence effect creates a variation of about $\pm$1,000 N, but this variation is only noticeable when the blade is affected by the wake behind the connecting linkage. In the Z-direction, the turbulence effect is negligible. Overall, the turbulence effect accounts for only 0.3 % of the overall change in force, being negligible in the design of turbine [5, 6].

3.5.3 Dual-Rotor Effect

The GST has two rotors of the same geometric dimension that rotate in opposite directions to balance the torques generated by the rotors. However, when the rotors rotate in difference phases, the force fluctuations caused by tower shadow effect cannot be offset. As a result, the power output and the turbine performance will be influenced by the phase difference between two rotors.

To examine this so-called dual-rotor effect, we examine the variation of the force exerted on the turbine under different phase shift between two rotors. Since in the present analysis only half of the turbine is considered due to its geometric symmetry, we shall use the data of Fig. 3.5 and superpose two sets of data of different phases. Given that the rotors have three blades, the force variation will repeat in every 120°. Furthermore, due to the symmetry between two blades, for example, the result under a 50° phase difference shall be the same as the result under a 70° phase difference, we need only to consider the phase difference ranging from 0° to 60° to account for an entire cycle of force variation.

Figure 3.13 presents the force variations for six phase differences ranging from 0° to 60°. Results show that, in terms of the force fluctuation, the greatest fluctuation occurs at the case of zero phase difference, and the smallest fluctuation occurs when the phase difference is 20°. In terms of average force, virtually all the cases end up with an average of about 735 kN for the dual-rotor turbine. This is also seen from the results shown in Fig. 3.14, in which the average forces for different phase differences are presented. More precisely to say, in a 120°-cycle, the average force exerted on the turbine is the greatest when the phase difference is 60°, and the smallest when the phase difference is either 0° or 120°. Please note that the minimum standard deviations occur for the cases of 30° and 90°, implying that these two cases have the smallest force exerted on the turbine. In other words, an optimized design for reducing the dual-rotor effect is to adopt 30° and 90° phase

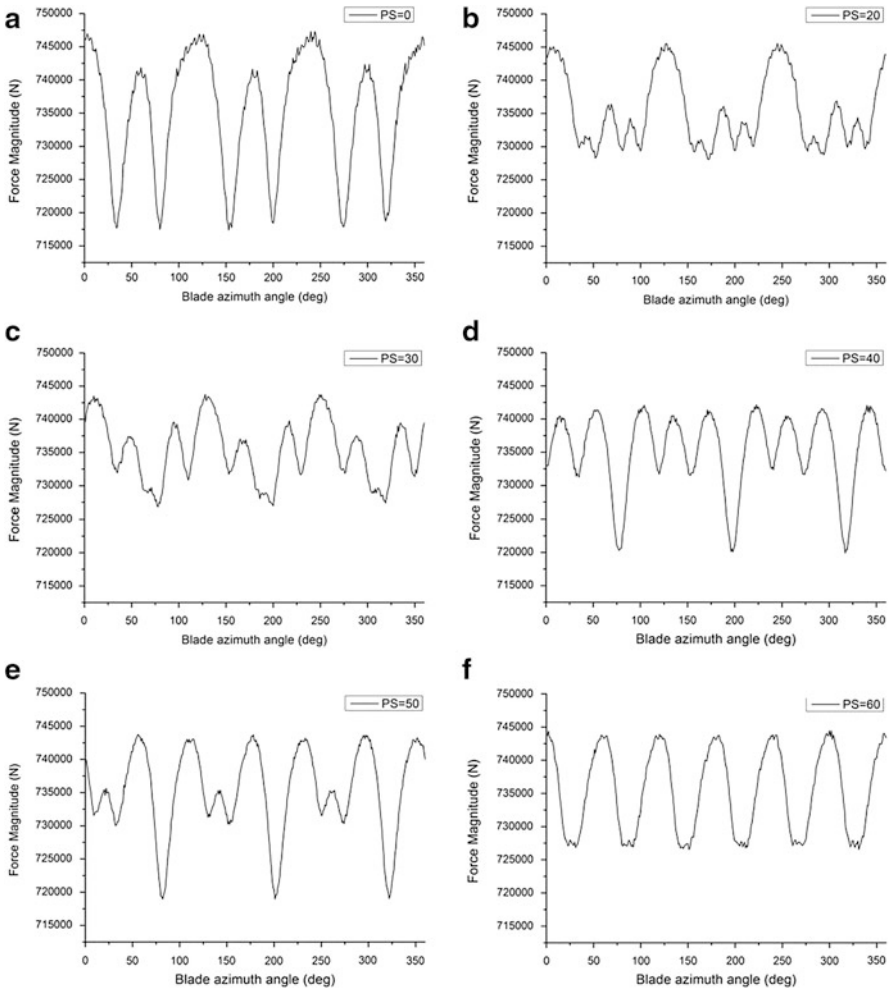

Fig. 3.13 The variation of force exerted on GST under various phase differences (the dual-rotor effect). (**a**) The phase difference is 0°; (**b**) 10°; (**c**) 30°; (**d**) 40°; (**e**) 50°; (**f**) 60°

differences, rather than a zero phase difference (or symmetric) condition. Nevertheless, the largest magnitude of variation is within ±7,800 N which accounts for only 1 % of the total force, implying that the dual-rotor effect due to the phase difference has insignificant influence on the turbine performance.

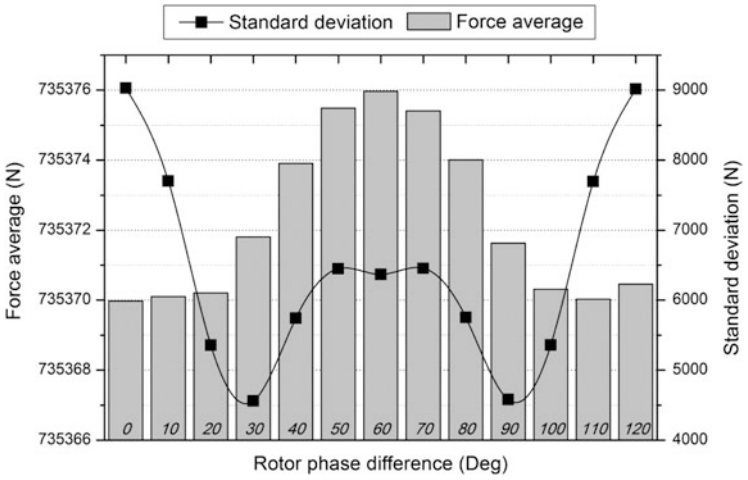

Fig. 3.14 The averaged force and the standard variation of the cyclic change for different phase differences

3.5.4 Cavitation Effect

When the angular speed of the blade exceeds beyond a critical value such that the local pressure on the blade falls below the vapor pressure, a vapor bubble will form on the blade. And then the vapor pressure of the bubble increases continuously due to the vapor accumulation inside the bubble. As the pressure becomes greater than the pressure of surrounding water, it triggers an explosion which often causes serious damage to the blade surface and reduces turbine performance. This effect is referred to as cavitation [19–21].

Figure 3.15 shows that, given $U = 1.2$ m/s, the minimum blade pressure occurring on the tip of the blade changes violently with the blade angle from -216 to -226 kPa. As compared with the threshold pressure of cavitation, as shown in the table below the curve in Fig. 3.15, results suggest that the tip of the blade shall never be at a position less than about 15 m in depth. In other words, as the rotor diameter of GST is 23 m, this result suggests that the turbine axis shall be positioned in the water at 30 m deep or more, so that the tip of the blade will never be in a position less than 20 m deep and the potential occurrence of cavitation can be prevented.

3.6 Comparison of CFD and BEM Results

To verify the reliability of the CFD results shown above, the so-called boundary element method (or BEM) is employed to calculate the blade force and torque of GST. The calculation conditions are the same as those of previous sections:

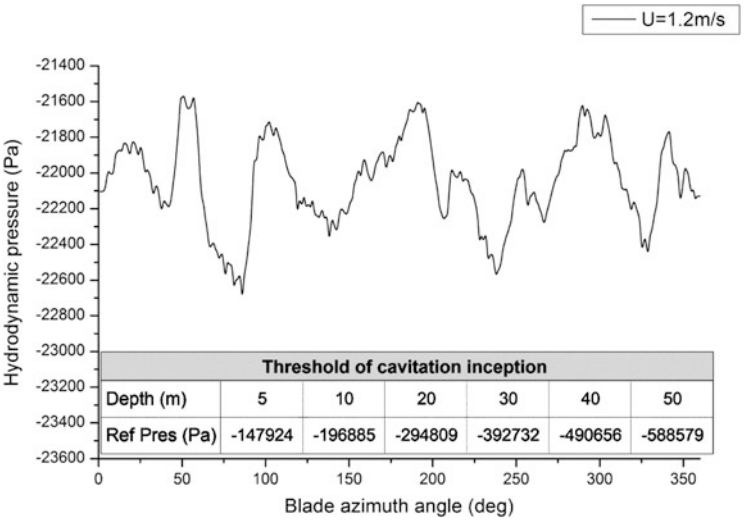

Fig. 3.15 The GST blade surface's minimum dynamic pressure fluctuates with the blade's azimuthal angle. The minimum pressure commonly occurs at the blade tip due to its highest tangential velocity

$U = 1.4$ m/s and $\Omega = 6$ rpm. We divide the blades into 1,000 elements and calculate the force of each element and then the torque with respect to the center of rotation. And the results are used to compare with previous CFD results.

Results showed that, by using CFD, the force on the blades in the X-direction is $-344{,}135$N while that is $-410{,}817$N when BEM is employed. The larger BEM results are attributed to the fact that the BEM calculations do not include either the tower shadow effect or the turbulence effect; both have negative contribution on the force exerted on the blade. In addition, CFD takes into account the friction loss of the flow, which is neglected by BEM. Therefore, the fact that the CFD results are about 16 % smaller than the BEM results is reasonable [20].

The above two methods are also used to calculate turbine performance for comparison with the data from Marine Current Turbine, Inc. [16], and the results are shown in Table 3.1. Comparison results show that, given $U = 1.4$ m/s, the CFD and BEM respectively end up with the turbine power output to be 0.237 MW and 0.227 MW, respectively. However, the power output measured by MCT falls between 0.174 and 0.207 MW. This is possibly due to that the MCT data are obtained by actual operational in situ and that the theoretical computations may have neglected some potential factors leading to power loss to some extent. Another possibility may stem from that a different blade is used in this study, which shows a better turbine performance.

In Table 3.1, we also compare the previous data with the so-called Betz limit, the theoretical maximum power output for water turbines. Among the examples given in the table, for the case of $U = 1.4$ m/s, for example, the power outputs of GST from CFD and BEM are respectively 0.237 MW and 0.227 MW, about 25 % and

Table 3.1 Comparison of results from CFD and BEM for the turbines GST and MCT

	GST ($U = 1.4$ m/s)		MCT [16]	
	CFD	BEM	$U = 1.4$ m/s	$U = 2.5$ m/s
C_P	0.442	0.423	0.403–0.481	
Power (MW)	0.237	0.227	0.174–0.207	0.99–1.18
Power (MW) according to Betz limit	0.318		0.256	1.455

40 % respectively less than Betz limit 0.318 MW. The power output of MCT lies within 0.174–0.207 MW, which is about 19–32 % less than Betz limit 0.256 MW. In addition, the C_p values of both GST and MCT can reach as high as 70 % of the limit, showing both designs are of good performance.

3.7 Design of Tail-Wing Stabilizer

To analyze the dynamical effects of the tail-wing stabilizer, we consider a Cartesian Coordinate that the origin is fixed at the center of the base linkage (or point K in Fig. 3.1c), the flow direction is opposite to the X-axis, the vertical direction is the same as that of the Z-axis, and the horizontal direction is parallel to the Y-axis, as shown in Fig. 3.3. Accordingly, the torque with respect to the X-axis is responsible for rolling motion, that to the Y-axis is for pitching motion, and that to the Z-axis is for yawing motion.

Considering that the point K is the cable support point (or the pivot point) of the fuselage, the variation of the torque exerted on the turbine by a single rotor is shown in Fig. 3.16. Results show that the pitching, rolling, and yawing torques are averaged respectively at about -0.3, 0.4, and 4.4 MN-m under the action of the Kuroshio flowing with a velocity of 1.4 m/s, while all fluctuate periodically in every 120°. As two rotors are considered simultaneously, the torques for rolling and yawing are expected to decrease dramatically due to the symmetry of the two rotors. If under some circumstances this symmetry is violated, the design of tail-wing stabilizer will serve to resume the designed altitude (or a horizontal altitude facing against the current) of the turbine in a reasonable time. In the following, the stabilizing mechanism applied by the tail-wing in three axes will be discussed.

3.7.1 Stability on the Rolling Plane

As shown in Fig. 3.17, the torque causing rolling motion (or the rolling torque) can be accounted for by the following relation:

$$Q_x = rF_b \sin\theta, \tag{3.1}$$

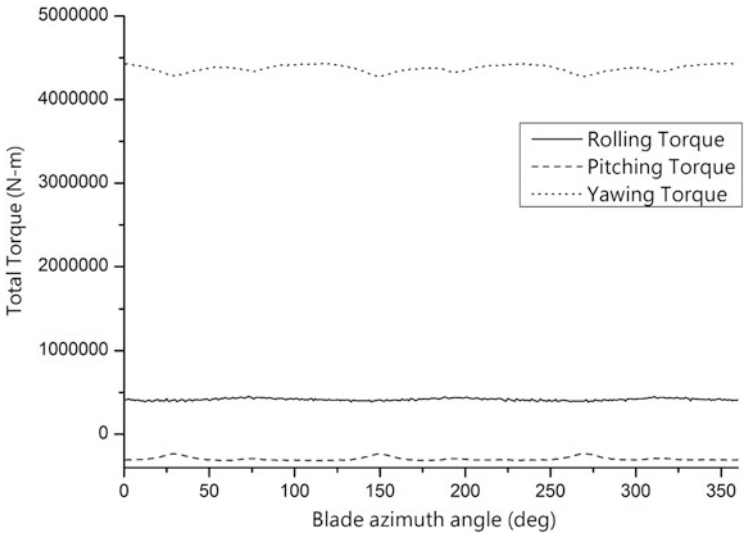

Fig. 3.16 The total torque in rolling, pitching, and yawing planes of a single-rotor turbine. The rolling, pitching, and yawing planes are referred to the coordinate system in Fig. 3.3

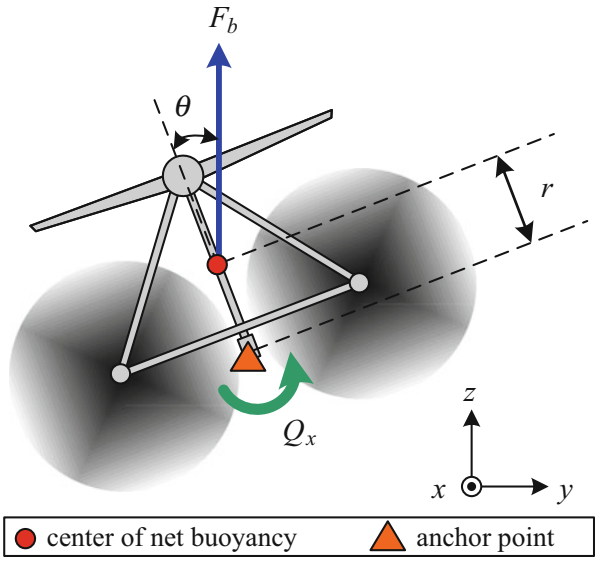

Fig. 3.17 The schematic diagram of the torque and force on the rolling plane

where Q_x is the rolling torque, r is the distance between the anchor point K and the center of the buoyancy, θ is the rolling angle, and F_b is the buoyancy. In a normal situation, the rolling angle is zero and the GST is anchored stably with a vertical altitude. As a perturbation is applied to cause a nonzero rolling angle, which may be

due to the turbulent flow impact on GST from one side or because the torques of the two rotors are not the same, the anti-rolling torque will be generated automatically due to the design shown in Fig. 3.17, i.e., the center of buoyancy locates above the anchor point. In such a design, as the buoyancy force is fixed as a prerequisite, the magnitude of anti-rolling torque is mainly dependent on the vertical distance between the anchor point K and the center of buoyancy, or r of (3.1). A larger distance leads to a larger anti-rolling torque and a more stable GST against the rolling motion.

To illustrate quantitatively the anti-rolling torque required to stabilize the rolling motion, we consider an example by considering the case of buoyancy force $F_b = 1.30$ MN, which is required to maintain the cable anchoring the turbine at an inclined angle 60° with respect to the horizontal plane. This buoyancy is also used in Sect. 3.9 to determine the mechanical property of the cable, and also used in Chap. 4 to analyze the structure stiffness of the relay platform. Under the action of this buoyancy, the relation between Q_x, r, and θ is shown in Fig. 3.18. For a constant r, which shall be constant when the turbine design is done, the anti-rolling torque Q_x increases as the rolling angle θ becomes larger. For a constant θ, similarly, the Q_x also increases with r, implying that for a larger turbine having a greater distance between anchor point and center of buoyancy, one needs a larger anti-rolling torque to resume the rolling motion.

The results in Fig. 3.18 can also be interpreted from a different viewpoint. As one had seen from Fig. 3.16, the maximum rolling torque resulting from a single rotor is about 452,000 Nm. We assume that there is a perturbation causing a net rolling torque about 10 % of the maximum value, i.e., 45,200 Nm, which may be due to fact that the flow velocities impinging on the two rotors become different, generating a rolling torque leading to a rolling motion. Under such a situation, we investigate four cases of different buoyancy to calculate the maximum-allowed (or the critical) rolling angle, beyond which the turbine will turn over, for five different r. Results shown in Table 3.2 indicate that for a constant r the critical rolling angle decreases as buoyancy increases. It also shows that for a constant buoyancy, the critical rolling angle decreases as r increases. Both results indicate that, for a larger turbine having a larger buoyancy and a longer r, the critical rolling angle is smaller, implying that the stability on the rolling plane is requested in a more restrictive manner.

3.7.2 Stability on the Pitching Plane

The stability on the pitching plane of GST (as shown in Fig. 3.19) is controlled by the vertical distance r between the anchored point and the center of buoyancy and the horizontal distance l between the anchored point to the hydrodynamic center of the horizontal stabilizer (or the tail-wing). As shown in Fig. 3.19, as pitching occurs to the GST, which can be due to the flow disturbance from below, the torque required to resume the designed altitude shall satisfy the following relation or beyond:

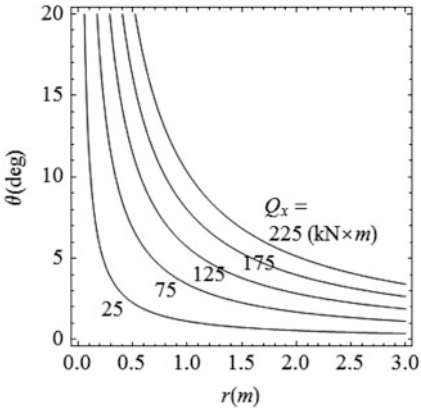

Fig. 3.18 The inverse proportion relation between rolling angle and the distance from anchoring point to center of buoyancy under the action of rolling torque. The buoyancy is $F_b = 1.26$ MN

Table 3.2 The critical rolling angles under different buoyancy and different distance from anchor point to center of buoyancy

	$F_b = 500$ kN	$F_b = 800$ kN	$F_b = 1{,}300$ kN	$F_b = 2{,}000$ kN
r (m)	θ (°)			
0.2	26.84	16.39	10.00	6.48
0.5	10.40	6.48	3.98	2.59
1.0	5.18	3.24	1.99	1.29
1.5	3.45	2.16	1.33	0.86
2.0	2.59	1.62	1.00	0.65

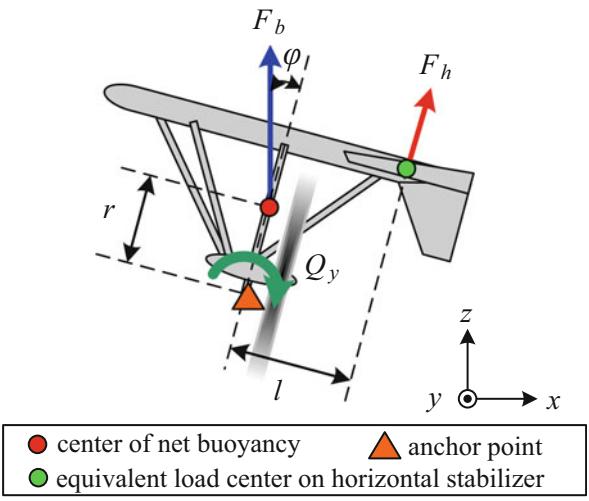

Fig. 3.19 The schematic diagram of the torque and force on the pitching plane

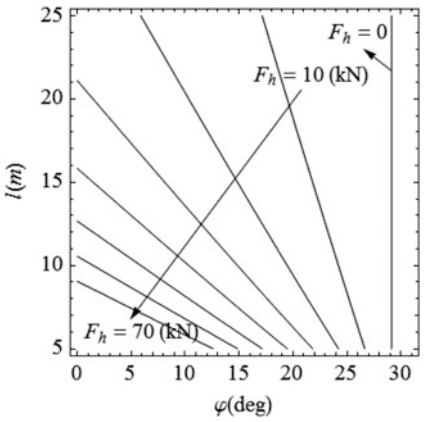

Fig. 3.20 The inverse linear relation between the pitching angle and the distance from anchoring point to hydrodynamic center of the horizontal stabilizer ($r = 1$ m and $F_b = 1{,}300$ kN)

$$Q_y = rF_b \sin\varphi + lF_h, \tag{3.2}$$

where Q_y is the pitching torque, φ is the pitching angle, and F_h is the equivalent load on the horizontal stabilizer.

To analyze the stability on the pitching plane, we consider that the GST is designed with $r = 1$ m and $F_b = 1{,}300$ kN and the turbine is disturbed by a pitching torque of about 633,000 Nm, which is two times the maximum pitching torque of a single rotor shown in Fig. 3.16. We then calculate F_h for various φ and l and the results are shown in Fig. 3.20. It is seen that, for a constant l, the F_h required to resume the turbine's horizontal altitude decreases as the pitching angle φ increases, implying that the function of the horizontal stabilizer is gradually taken over by the buoyancy as φ increases. And this function is completely vanished when φ becomes larger than 29°, as shown in the vertical line of $F_h = 0$ in Fig. 3.20. On the other hand, for a constant φ, the F_h decreases as l increases, implying that the stability on the pitching plane is higher for a larger turbine (of a larger l).

Results of Fig. 3.20 also indicate that, to maintain the altitude of GST horizontally (or $\varphi = 0$), the F_h required increases for a smaller l. That means the horizontal stabilizer is still needed to provide a lift force to equilibrate the pitching moment 633,000 Nm applied by the flow acting on the turbine. Consequently, the horizontal stabilizer of GST is better designed with a shape of airfoil which would provide a lift force (of about 633,000 Nm) when the angle of attack is zero. For the turbine of $l = 15$ m, for example, the lift force shall be as large as 42 kN, as shown in Fig. 3.20.

Table 3.3 shows the maximum-allowed (or critical) pitching angle for a turbine with prerequisite specifications $r = 1$ m and $F_b = 1{,}300$ kN under different designs of horizontal stabilizer accounted for by the parameters l and F_h. For the case of $l = 15$ m and $F_h = 35$ kN, for example, the critical pitching angle is 4.77°, which means the turbine would become unstable on the pitching plane as the pitching angle increases to 5° or beyond. It turns out that this is a dangerous design due to a

Table 3.3 The critical pitching angles for different equivalent load on the horizontal stabilizer with different distance from anchor point to hydrodynamic center of the horizontal stabilizer ($r = 1$ m and $F_b = 1{,}300$ kN)

	$F_h = 15$ kN	$F_h = 20$ kN	$F_h = 35$ kN	$F_h = 50$ kN
l (m)	φ (°)			
5	25.43	24.21	20.64	17.14
10	21.82	19.46	12.58	5.88
15	18.30	14.85	4.77	–
20	14.85	10.33	–	–
25	11.45	5.88	–	–

small critical pitching angle. Accordingly, one shall redesign the horizontal stabilizer by, for example, shortening the distance l to 10 m to increase the critical pitching angle up to 12.58°, or to 5 m to get a larger critical pitching angle 20.64°. For this case, a larger lift force would reduce the critical pitching angle, making the turbine more unstable. Conclusively, a smaller turbine (of a smaller l) is more stable on the pitching plane because it has a larger critical pitching angle.

To design the horizontal stabilizer for the determination of both l and F_h, one shall calculate the effective area of the horizontal stabilizer. To do this, we start from the force diagram shown in Fig. 3.21, the lift force (F_l) and the drag force (F_d) are obtained as

$$F_l^{(h)} = F_h \cos\varphi = \frac{1}{2} C_l^{(h)} \rho U^2 A_h, \tag{3.3}$$

$$F_d^{(h)} = F_h \sin\varphi = \frac{1}{2} C_d^{(h)} \rho U^2 A_h, \tag{3.4}$$

where the superscript h denotes the horizontal stabilizer, $C_l^{(h)}$ and $C_d^{(h)}$ are respectively the lift and drag coefficients, A_h is the effective area of the horizontal stabilizer, and ρ and U are the seawater density and the flow velocity referring to Sect. 3.4.

Rewriting (3.3) and (3.4), with the aid of (3.2), gives

$$\left|2\left(Q_y - rF_b \sin\varphi\right)\cos\varphi\right| = lC_l \rho U^2 A_h, \tag{3.5}$$

$$\left|2\left(Q_y - rF_b \sin\varphi\right)\sin\varphi\right| = lC_d \rho U^2 A_h, \tag{3.6}$$

By assuming that $Q_y = 633{,}000$ kN, $r = 1$ m, $F_b = 1{,}300$ kN, $l = 15$ m, $\rho = 1{,}030$ kg/m^3, and $U = 1.4$ m/s, the A_h is calculated for various $C_l^{(h)}$ and $C_d^{(h)}$ at different pitching angles, and the results are shown in Fig. 3.22. As one can see from Fig. 3.22a, for a constant $C_l^{(h)}$ (or a constant lift force), the effective area needed is smaller for a larger critical pitching angle. This is reasonable that a turbine of a larger critical pitching angle is more stable by design; it accordingly needs a stabilizer of smaller area. For a constant critical pitching angle, a larger

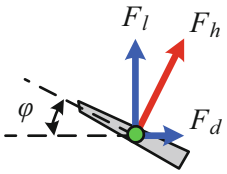

Fig. 3.21 The schematic diagram of the forces acting on the horizontal stabilizer

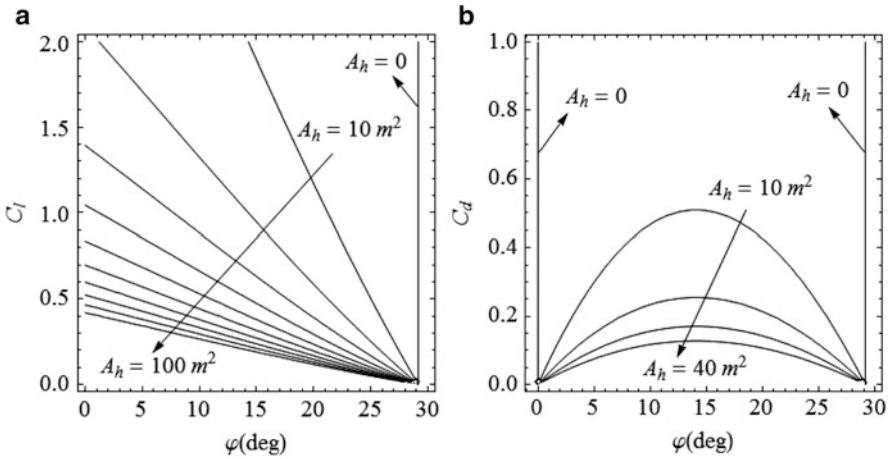

Fig. 3.22 (**a**) The inverse linear relation between the pitching angle and the lift coefficient for different effective areas of the horizontal stabilizer. (**b**) The relation between the pitching angle and the drag coefficient for different effective areas of the horizontal stabilizer ($r = 1$ m, $F_b = 1{,}300$ kN, $l = 15$ m, $\rho = 1{,}030$ kg/m^3, and $U = 1.4$ m/s)

A_h (or a larger horizontal stabilizer) is accompanied with a smaller $C_l^{(h)}$ (or an airfoil with a smaller camber) to generate a pitching moment to counteract with the applied torque Q_y.

On the other hand, the drag force of the stabilizer shall be designed with a smallest value to decrease the loading on the anchoring cable. Results shown in Fig. 3.22b suggest that at a pitching angle of either 0° or 30°, the drag force on the tail-wing vanishes. For the pitching angle being between 0° and 30°, the maximum drag force occurs at the pitching angle equal to 15°, and the drag force decreases with increasing effective area of stabilizer.

According to White [22], theoretically, for a flat-plate horizontal stabilizer, the lift coefficient $C_l^{(h)}$ for a 5° pitching angle is about 0.55. Thus, according to the results shown in Fig. 3.22a [or Eq. (3.6)], the overall effective area of the horizontal stabilizer can be obtained as 62 m^2. Since the stabilizer is composed of two symmetric horizontal plates, the area of each plate is 31 m^2. Meanwhile, the drag coefficient $C_d^{(h)}$ can be obtained as 0.048 from Fig. 3.22b or Eq. (3.6). On the contrary, if an effective area of the horizontal stabilizer is known as a prerequisite,

Table 3.4 The demand flat-plate horizontal stabilizer areas with their lift and drag coefficients for different given pitching angles ($r = 1$ m, $F_b = 1{,}300$ kN, $l = 15$ m, $\rho = 1{,}030$ kg/m^3, and $U = 1.4$ m/s)

φ (°)	$C_l^{(h)}$ [22]	$C_d^{(h)}$	A_h (m^2)
5	0.55	0.05	62.46
10	1.09	0.12	24.29
15	1.63	0.26	11.64
20	2.15	0.55	5.44
25	2.66	1.59	1.89

both the lift and drag coefficients for different pitching angles can be also obtained from Fig. 3.22.

We choose five different pitching angles and calculate the lift coefficient, the drag coefficient, and the effective area of the flat-plate stabilizer, and the relevant data are shown in Table 3.4. In general, after the pitching moment $Q_y = 633{,}000$ kN is applied on the turbine, both the lift and drag forces required to counteract with this acting torque increase as the pitching angle is larger, while the effective area can be designed with a smaller value. Results of Table 3.4 can also be interpreted from another viewpoint that, as the pitching motion is generated, the drag and lift force shall increase as the pitching angle is enlarged, making the turbine more unstable unconditionally. This may develop into a disaster which shall be avoided in any circumstance. To prevent this disaster, one may consider to use a stabilizer of larger effective area to ensure smaller drag and lift forces.

3.7.3 Stability on the Yawing Plane

The torque leading to an instability on the yawing plane is the moment caused by the forces applied on the GST with respect to Z-axis. This moment may be generated by the imbalance between the forces applied on the two rotors, and which shall be balanced by the torque applied by the hydrodynamic load on the rudder (or the vertical stabilizer) to damp out the yawing motion in a short period.

As shown in Fig. 3.23, in general, the stability on the yawing plane of GST is controlled by the distance between the anchoring point to the hydrodynamic center on the rudder and the force applied on the rudder. To recover the yawing configuration, the torque satisfies

$$Q_z = dF_v, \tag{3.7}$$

where Q_z is the yawing torque, F_v is the equivalent load on the rudder, and d is the horizontal distance between the anchoring point pivot and the hydrodynamic center of the rudder. The thrust and drag forces computed form the equivalent load on the rudder are

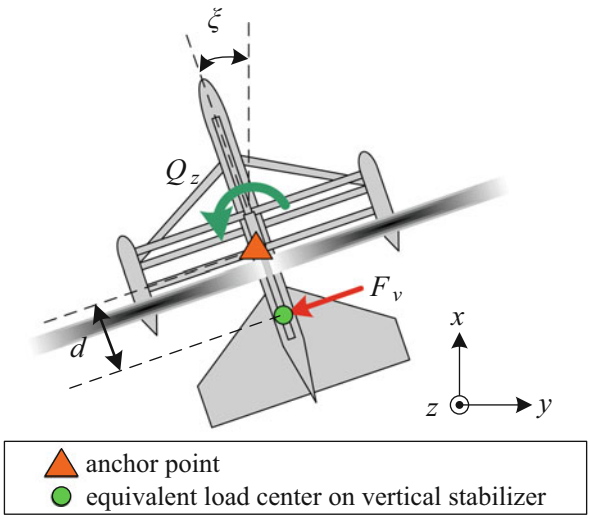

Fig. 3.23 The schematic diagram of the force and torque on the yawing plane

$$F_{\mathrm{l}}^{(v)} = F_v \cos\xi = \frac{1}{2} C_{\mathrm{l}}^{(v)} \rho U^2 A_v, \tag{3.8}$$

$$F_{\mathrm{d}}^{(v)} = F_v \sin\xi = \frac{1}{2} C_{\mathrm{d}}^{(v)} \rho U^2 A_v, \tag{3.9}$$

where the superscript v denotes the horizontal stabilizer, $C_{\mathrm{l}}^{(v)}$ and $C_{\mathrm{d}}^{(v)}$ are the thrust and drag coefficients, ξ is the yawing angle, and A_v is the effective area of the vertical stabilizer.

Results of Fig. 3.16 show that the maximum yawing torque on a single rotor is about 4,436,000 Nm. For the GST having two rotors, we assume that there is a 5 % of the maximum yawing torque applied on GST, namely, $Q_z = 221{,}800$ Nm, and $d = 15$ m is chosen for the design, the equivalent load needed to apply on the rudder to prevent yawing is $F_v = 14.79$ kN. For the given yawing torque above, the equivalent load on the rudder is inversely proportional to the distance, as shown in Fig. 3.24.

To design the rudder in terms of hydrodynamic characteristics and the geometry, we consider the following equations derived from (3.8) and (3.9), with the aid of (3.7), yielding

$$|2Q_z \cos\xi| = dC_{\mathrm{l}}^{(v)} \rho U^2 A_v, \tag{3.10}$$

$$|2Q_z \sin\xi| = dC_{\mathrm{d}}^{(v)} \rho U^2 A_v. \tag{3.11}$$

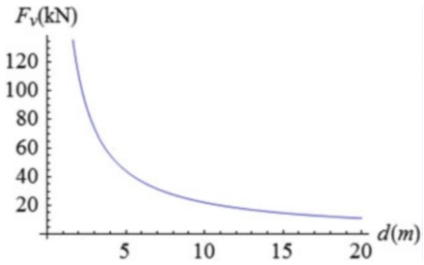

Fig. 3.24 The demand equivalent load on the vertical stabilizer versus the horizontal distance from anchoring point to the hydrodynamic center of the rudder

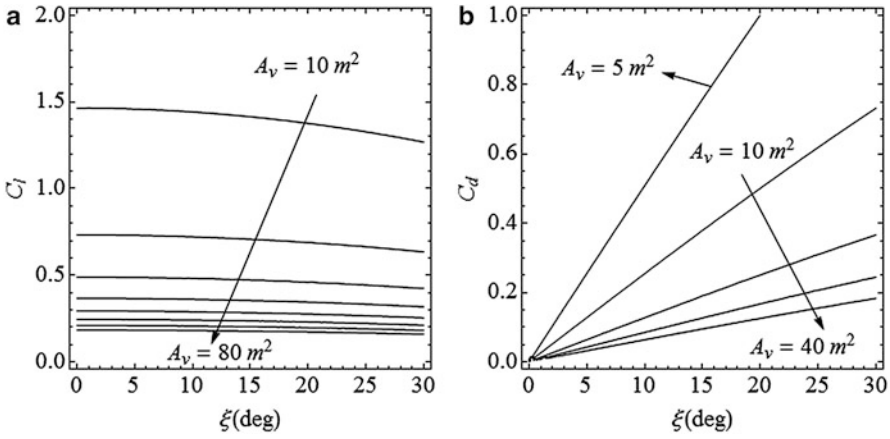

Fig. 3.25 (**a**) The linear relation between the yawing angle and the lift coefficient for different effective areas of the rudder. (**b**) The linear proportion relation between the yawing angle and the drag coefficient for different effective areas of the rudder ($d = 15$ m, $\rho = 1{,}030$ kg/m^3, and $U = 1.4$ m/s)

By assuming that $Q_z = 221{,}800$ Nm, $d = 15$ m, $\rho = 1{,}030$ kg/m^3, and $U = 1.4$ m/s, the lift and drag coefficients with respect to yawing angle for rudders of various area are shown in Fig. 3.25.

Results shown in Fig. 3.25 indicate that, by giving a critical yawing angle which accounts for the maximum yawing angle the GST will allow in response to various disturbances, both the lift and drag coefficients of the rudder shall decrease for a rudder of larger area. On the other hand, for a given area of the rudder, the lift coefficient virtually remains the same with respect to varying yawing angle, while the drag coefficient increases linearly with the yawing angle monotonically.

If a flat-plate rudder is considered, as discussed in previous sections, the lift coefficient for a 5° yawing angle is about 0.55 [22]. Results shown in Fig. 3.25a give that the effective area of the rudder is 27 m^2 and those of Fig. 3.25b give that the drag coefficient is obtained to be 0.048. To more clearly illustrate the design parameters for a flat-plate rudder, we summarize in Table 3.5 the results for five yawing

Table 3.5 The demand flat-plate rudder areas with their lift and drag coefficients for different given yawing angles ($Q_z = 221{,}800$ Nm, $d = 15$ m, $\rho = 1{,}030$ kg/m^3, and $U = 1.4$ m/s)

φ (°)	$C_l^{(v)}$ [22]	$C_d^{(v)}$	A_v (m^2)
5	0.55	0.05	26.65
10	1.09	0.10	13.38
15	1.63	0.14	8.97
20	2.15	0.19	6.79
25	2.66	0.23	5.50

angles under the conditions $Q_z = 221{,}800$ Nm, $d = 15$ m, $\rho = 1{,}030$ kg/m^3, and $U = 1.4$ m/s. Results indicate that, for a GST of a larger critical yawing angle, which means the turbine is more stable on the yawing plane, one shall have a rudder of smaller area while having both larger lift and drag coefficients. On the other hand, as a rudder of larger area is considered, the critical yawing angle is smaller, which means the turbine is less stable on the yawing plane.

3.8 Selection of Turbine Anchor Point

The original design of GST is to anchor the turbine on the point K of Fig. 3.1 [1], which is a single-cable anchoring system, having advantages that the turbine has more degree of freedom to move in three axes and the cost of construction engineering is significantly lower. For different kind of turbine, such as the turbine considered for the Gulf Stream in Florida [23, 24], a different anchoring system shall be considered to secure the stability of the turbine under the action of strong current.

The analyses of turbine dynamics for the case considering anchoring the turbine on the point K have been done in previous sections, and the dynamic characteristics of the GST have been illustrated in detail. There are, however, many other options for anchoring at different points on the turbine, such as those shown in Fig. 3.26. For a different anchoring system, the dynamic characteristics of the turbine shall be different from those anchoring on the point K. As shown in Fig. 3.27 regarding the overall torque applied on the turbine, results illustrate that the dynamic characteristics of the turbine are very different from each other for the cases of different anchoring points considered.

For case B anchoring the GST on the nose of main pontoon, for example, the overall torque is about 50 % higher than that of the case A anchoring on Point K, which is because the torque is dependent with the distance between the anchoring point and the hydrodynamic center on the turbine, and anchoring on the nose of pontoon increases the distance by more than 50 %. For case C anchoring the GST on the noses of the watertight nacelles by two cables, the overall torque is reduced to about one-ninth of that of case A. This is because, due to anchoring by two cables on the two sides of the turbine, both the rolling and yawing motions are restricted to a limited range so that the torques needed to secure the stability on the rolling and yawing planes are reduced to a very low level. For the stability on the pitching plane, the pitching torque is also reduced since the distance between the anchoring

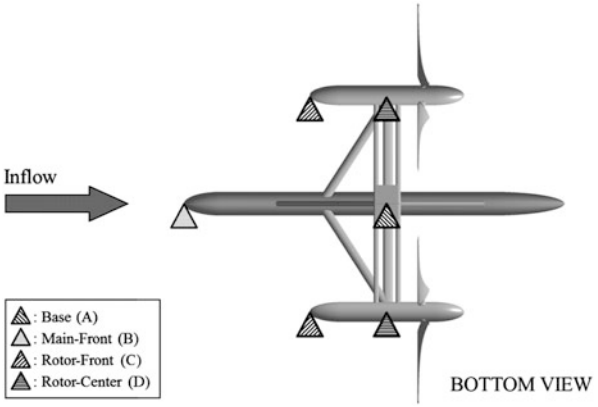

Fig. 3.26 Four types of the anchoring point selection: (**a**) the *center* of the base (point K in Fig. 3.1c); (**b**) the *nose* of the main pontoon; (**c**) the *nose* of the watertight nacelle; (**d**) the *bottom center* beneath the watertight nacelle

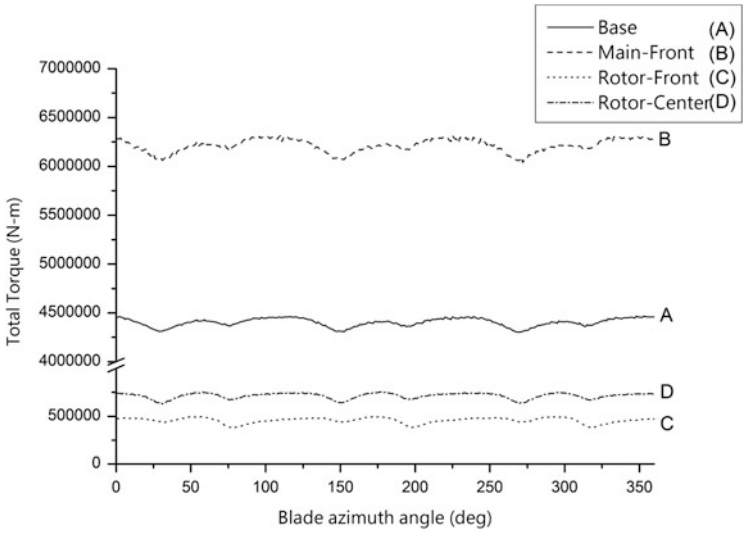

Fig. 3.27 The total torque with different blade azimuthal angles for the four types of the anchoring point selection

point and the hydrodynamic center on the horizontal stabilizer is increased compared to that of case A.

The last case considered is to anchor the turbine by two cables on the center of the bottom of the two nacelles, i.e., the case D. From the fact that the two anchoring points of this case are close to those of case C and that this case also features with two cables anchoring on the two sides of the turbine, one may imply that the hydrodynamic characteristics and the overall torque of the turbine of case D are similar to those of case C, and this is confirmed by the results shown in Fig. 3.27.

Table 3.6 Physical and material properties of various types of cable for anchoring the GST onto the relay platform

	Density (kg/m^3)	Elasticity coeff. (GPa)	Tensile strength (GPa)	Ductility (%)	Source
Nylon	1,120–1,160	2.00–4.00	0.06–0.08	90.0	[a]
	1,140	5.50	0.85	18.0	[b]
	1,060–1,140	2.07–2.41	0.05–0.07	20.0–60.0	[c]
	1,140	–	–	18.0–25.0	[d]
	1,040–1,140	–	0.04–0.06	150.0–400.0	[e]
	1,140	–	–	15.0–28.0	[f]
	1,140	0.87	0.2	–	[g]
Steel	7,700–8,030	200–205	0.40–0.59	–	[a]
	7,860	200	2.16	1.1	[b]
	7,850	210	1.40	–	[g]
PET	1,360	2.00–2.70	0.06	–	[a]
	1,380	9.00	1.05	12.5	[b]
	1,380	3.24	0.08	45.0	[c]
	1,380	–	–	12.0–15.0	[d]
	1,270	–	0.07	110.0	[e]
	1,380	–	–	12.0–15.0	[f]
	1,380	1.6–10	0.20–0.50	–	[g]
PP	900–1,240	1.30–2.00	0.03–0.04	–	[a]
	910	4.20	0.50	12.0	[b]
	890–1,270	0.03–0.7	0.02–0.10	1.5–600.0	[c]
	910	–	–	15.0–25.0	[d]
	900	–	0.03	200.0	[e]
	910	–	–	18.0–22.0	[f]
	910	–	–	–	[g]

[a] http://www.engineeringtoolbox.com/
[b] http://www.offshoreengineering.org/
[c] http://www.sdplastics.com/
[d] http://www.erinrope.com/
[e] http://breezeplastics.com/
[f] http://www.gpjrope.com/
[g] http://www.tensiontech.com/

3.9 Turbine Cable Selection

As mentioned earlier, GST was selected as the basis for analysis because the turbines feature a self-stabilizing balancing device which allows for a single cable to be connected to the center point of the turbine's base (point K in Fig. 3.1c) which is then anchored to the relay platform. Many types of cables fulfill the requirements of high tension and high elongation including nylon rope, steel rope, polyester rope (PET), and polypropylene rope (PP) (see Table 3.6 for their respective mechanical and physical properties). PET is slightly heavier than seawater, has a high tensile strength (second only to steel rope), and is highly stretchable (second only to nylon rope). These advantages make PET rope a good choice for anchoring the turbine. Yet another advantage is that different weaving methods can

be used to produce a variety of cable diameters to meet the requirements of specific design specification; see please Appendix D for more details.

Analysis results for cable force shown in Fig. 3.5 show that, given $U = 1.4$ m/s and $\Omega = 6$ rpm, the averaged current thrust acting on GST is 735 kN, with a standard deviation of 4.5 kN–9 kN. Therefore, the thrust acting on the turbine in the horizontal direction can be as high as 744 kN or more. In calculating the total force of the cable, in addition to the above-mentioned current thrust, the turbine's floating buoyancy in the vertical direction must also be taken into account. We assume that the buoyancy force is 1,270 kN and thrust force is 735 kN so that the combined force is 1,470 kN with an inclined angle of 60° with respect to the horizontal axis. In the marine engineering design, it is reasonable to consider a safety factor of 5, so the design value of the total cable force should be set to 7,350 kN. We will use this design value to select the size and material for the cable used to anchor the turbine.

Traditionally, the anchoring cables are of steel-based material. But, nonetheless, due to the weight and corrosion factors, steel-based cables are not suitable for anchoring Kuroshio turbines. New cables made of plastic composites or polymer compounds, usually being of lighter weight and of better mechanical properties, become the better choice. These cables are light and strong, and, more importantly, their hairy exteriors can reduce high-frequency vibrations caused by ocean flow, making them the best choice for anchoring turbines [25]. As the cable diameter is chosen to be 20 cm, given that the force applied on the cable is 7,350 kN, the tensile strength of the cable shall be 0.0581 GPa or more. As shown in Table 3.6, there are many cables such as nylon 1140, PET 1380, and PP 910 with tensile strength as high as 0.229 GPa or more, being much larger than the required tensile strength of the cable. If a two-cable anchoring system is considered, as cases C and D shown in Fig. 3.6, the required tensile strength of the cable is thus reduced by half to 0.0291 GPa. Consequently, the selection of the cable lies in a much larger range.

3.10 Overview of the GST Performance

The GST is equipped with two rotors, each with three 10 m-long blades rotating with an angular speed of 6 rpm. As it is under the action of 1.4 m/s Kuroshio flow, the total thrust applied on GST is about 735,000 kN and the power generated is about 0.5 MW. It can be anchored on the relay platform (will be discussed in Chap. 4) by a single cable, and is autonomously balancing in the rolling, yawing, and pitching planes by the design of the tail-wing stabilizer and the distance between hydrodynamic center and the anchoring point of the turbine. Analyses of present chapter have shown that this single-strand-anchored and autonomously balancing design has demonstrated superiority for the Kuroshio power plant, which is considered to be deployed in the ocean of several 100 m deep or more.

While the GST works under the action of Kuroshio, the exerted force shows a cyclic change due to the tower shadow effect, which is mainly the result caused by the disturbance of the wakes generated behind the connection linkage on the two

rotors. If we consider that GST is anchored by a cable having an inclination angle of 45 with respect to the horizontal direction, the total force (the net buoyancy combined with the thrust) can be as high as 1,500 kN, and the force amplitude varies within 6 % of the cyclic change. A single cable made of the nylon, PET, or PP with 20 cm in diameter can is strong enough to support GST securely on the relay platform of which the safety factor reaches five. If a dual cable anchored to both the noses of the watertight nacelles, the stability of GST on the rolling and yawing planes is greatly enhanced, and the specifications of the cable can be downgraded, and thus the cost can be saved for diminishing that resulted from the additional works.

The tower shadow effect is the major factor that causes the cyclic change of the turbine reaction force. The variation of this cyclic change may result in the fatigue failure in turbine components. However, the effect cannot be prevented if the connecting linkages are equipped at the upstream side of the rotor. A possibility to diminish the tower shadow effect is to move the rotor to the upstream of the linkages, such as at the nose of watertight nacelle. This change would require a new design of the autonomously balancing mechanism, which is controlled by the tail-wing stabilizer and the anchoring system.

References

1. Robson JH (2007) Submersible electrical power generating plant. US Patent 7291936B1, 6 Nov 2007
2. Batten WMJ, Bahaj AS, Molland AF, Chaplin JR (2008) The prediction of the hydrodynamic performance of marine current turbines. Renew Energy 33(5):1085–1096. doi:10.1016/j.renene.2007.05.043
3. ANSYS FLUENT 12.1 User Manual
4. Duque EPN, Burklund MD, Johnson W (2003) Navier–stokes and comprehensive analysis performance predictions of the NREL phase VI experiment. J Sol Energy Eng 125:457–467. doi:10.1115/1.1624088
5. Sørensen NN, Michelsen JA, Schreck S (2002) Navier–stokes predictions of the NREL phase VI rotor in the NASA Ames 80 ft × 120 f. wind tunnel. Wind Energy 5:151–169. doi:10.1002/we.64
6. Menter FR (1994) Two-equation eddy-viscosity turbulence models for engineering applications. AIAA J 32:1598–1605. doi:10.2514/3.12149
7. Wilcox DC (1993) Comparison of two-equation turbulence models for boundary layers with pressure gradient. AIAA J 31:1414–1421. doi:10.2514/3.11790
8. Patankar SV, Spalding DB (1972) A calculation procedure for heat, mass and momentum transfer in 3-dimensional parabolic flow. Int J Heat Mass Transf 15(10):1787–1806. doi:10.1016/0017-9310(72)90054-3
9. Turnock SR, Phillips AB, Banks J, Nicholls-Lee R (2011) Modelling tidal current turbine wakes using a coupled RANS-BEMT approach as a tool for analysing power capture of arrays of turbines. Ocean Eng 38(11–12):1300–1307. doi:10.1016/j.oceaneng.2011.05.018
10. Lee SH, Jang K, Lee J, Hurt N (2010) A numerical study for the optimal arrangement of ocean current turbine generators in the ocean current power parks. Curr Appl Phys 10:S137–S141. doi:10.1016/j.cap.2009.11.018

11. Myers LE, Bahaj AS (2010) Experimental analysis of the flow field around horizontal axis tidal turbines by use of scale mesh disk rotor simulators. Ocean Eng 37(2–3):218–227. doi:10.1016/j.oceaneng.2009.11.004
12. Harrison ME, Batton WMJ, Myers LE, Bahaj AS (2010) Comparison between CFD simulations and experiments for predicting the far wake of horizontal axis tidal turbines. Renew Power Gen 4(6):613–627. doi:10.1049/iet-rpg.2009.0193
13. Bahaj AS, Myers LE, Thompson G. Characterising the wake of horizontal axis marine current turbines. In: Proceedings of the 7th European wave and tidal energy conference, Porto, Portugal, 11–14 Sept 2007
14. Myers L, Bahaj AS (2007) Wake studies of a 1/30th scale horizontal axis marine current turbine. Ocean Eng 34:758–762. doi:10.1016/j.oceaneng.2006.04.013
15. Myers LE, Bahaj AS (2012) An experimental investigation simulating flow effects in first generation marine current energy converter arrays. Renew Energy 37(1):28–36. doi:10.1016/j.renene.2011.03.043
16. Bahaj AS, Batten WMJ, McCann G (2007) Experimental verifications of numerical predictions for the hydrodynamic performance of horizontal axis marine current turbines. Renew Energy 32(15):2479–2490. doi:10.1016/j.renene.2007.10.001
17. Bahaj AS, Molland AF, Chaplin JR (2007) Power and thrust measurements of marine current turbines under various hydrodynamic flow conditions in a cavitation tunnel and a towing tank. Renew Energy 32:407–426. doi:10.1016/j.renene.2006.01.012
18. Batten WMJ, Bahaj AS, Molland AF, Chaplin JR (2007) Experimentally validated numerical method for the hydrodynamic design of horizontal axis tidal turbines. Ocean Eng 34 (7):1013–1020. doi:10.1016/j.oceaneng.2006.04.008
19. Batten WMJ, Bahaj AS, Molland AF, Chaplin JR (2006) Hydrodynamics of marine current turbines. Renew Energy 31(2):249–256. doi:10.1016/j.renene.2005.08.020
20. Zanette J, Imbault D, Tourabi A (2010) A design methodology for cross flow water turbines. Renew Energy 35:997–1009. doi:10.1016/j.renene.2009.09.014
21. Goundar JN, Ahmed MR, Lee Y-H (2011) Numerical and experimental studies on hydrofoils for marine current turbines. Renew Energy 42:173–179. doi:10.1016/j.renene.2011.07.048
22. White FM (1999) Fluid mechanics, 4th edn. McGraw-Hall, New York
23. VanZwieten J, Driscoll FR, Leonessa A, Deane G (2006) Design of a prototype ocean current turbine—part I: mathematical modeling and dynamics simulation. Ocean Eng 33:1485–1521. doi:10.1016/j.oceaneng.2005.10.005
24. VanZwieten J, Driscoll FR, Leonessa A, Deane G (2006) Design of a prototype ocean current turbine—part II: flight control system. Ocean Eng 33:1522–1551. doi:10.1016/j.oceaneng.2005.10.006
25. Brown DT, Mavrakos S (1999) Comparative study on mooring line dynamic loading. Mar Struct 12(3):131–151. doi:10.1016/S0951-8339(99)00011-8